Original Article

Journal of Intelligent Material Systems and Structures

Journal of Intelligent Material Systems and Structures
2014, Vol. 25(14) 1664–1680
© The Author(s) 2014
Reprints and permissions:
sagepub.co.uk/journalsPermissions.nav
DOI: 10.1177/1045389X14544152
jim.sagepub.com
SAGE

Multiple patch–based broadband piezoelectric energy harvesting on plate-based structures

Ugur Aridogan[1], Ipek Basdogan[1] and Alper Erturk[2]

Abstract

Several engineering systems, such as aircraft structures, are composed of load-bearing thin plates that undergo vibrations and employ wireless health, usage, and condition monitoring components, which can be made self-powered using vibrational energy harvesting technologies. Integrated piezoelectric patches can be implemented for enabling self-powered sensors in the neighborhood of plate-based structures. In this work, coupled electroelastic modeling and experimental validations of broadband energy harvesting from structurally integrated piezoelectric patches on a rectangular thin plate are presented. A distributed-parameter electroelastic model for multiple patch–based energy harvesters attached on a thin plate is developed. Closed-form structural and electrical response expressions are derived for multiple vibration modes of a fully clamped thin plate for the series and parallel connection configurations of multiple patch–based energy harvesters. Experimental and analytical case studies are then compared for validating the analytical models of structurally integrated multiple patch–based energy harvesters. It is shown that analytical electroelastic frequency response functions exhibit very good agreement with the experimental frequency response function measurements for the series and parallel connection cases. In addition to offering an effective interface for energy harvesting from two-dimensional thin structures, series and parallel multiple patch–based energy harvester configurations yield effective broadband energy harvesting by combining the electrical outputs of harvester patches for multiple vibration modes.

Keywords

Vibrational energy harvesting, patch-based piezoelectric harvesters, electroelastic modeling, power output analysis, plate structures

Introduction

Vibrational energy harvesting has been extensively investigated over the past decade for powering wireless electronic components, such as sensor networks, used in a wide range of engineering applications (Beeby et al., 2006; Cook-Chennault et al., 2008b; Roundy et al., 2003). Several methods for vibration-to-electric energy conversion have been researched ranging from basic transduction principles (e.g. electromagnetic (Beeby et al., 2007; Zhu et al., 2012) and electrostatic (Chiu and Tseng, 2008; Lee et al., 2009)) to smart materials (e.g. piezoelectric (Anton and Sodano, 2007; Wang and Song, 2006), magnetostrictive (Wang and Yuan, 2008), electroactive (Brufau-Penella et al., 2008), and more recently combination of smart materials with metamaterial concepts (Carrara et al., 2013)). Among the implementations of these energy conversion methods in energy harvesting, piezoelectric transduction is the most popular one since piezoelectric materials have large power density comparable with lithium-ion-based storage systems and other regenerative energy technologies (Cook-Chennault et al., 2008a), and they can be manufactured in different geometries and at different scales (Anton and Sodano, 2007; Wang and Song, 2006).

Research in piezoelectric energy harvesting field has been mostly focused on cantilevered beams with piezoelectric layers, that is, unimorph or bimorph configurations. Analytical (Erturk et al., 2008; Erturk and Inman, 2008a; Erturk and Inman, 2009; Zhao and Erturk, 2013), semi-analytical (Erturk, 2012), and

[1]Department of Mechanical Engineering, College of Engineering, Koç University, Istanbul, Turkey
[2]The George W. Woodruff School of Mechanical Engineering, Georgia Institute of Technology, Atlanta, GA, USA

Corresponding author:
Ipek Basdogan, Department of Mechanical Engineering, College of Engineering, Koç University, 34450 Istanbul, Turkey.
Email: ibasdogan@ku.edu.tr

Downloaded from jim.sagepub.com at GEORGIA TECH LIBRARY on September 11, 2014

finite-element (Elvin and Elvin, 2009; Yang and Tang, 2009) models governing the coupled electromechanical behavior of cantilevered piezoelectric energy harvesters have been developed and validated experimentally (Erturk, 2012; Erturk et al., 2008; Erturk and Inman, 2009). Major modeling issues (Erturk and Inman, 2008b) and methods for performance enhancement (Erturk et al., 2009a, 2009b; Huang and Lin, 2012) have also been reported for cantilevered harvester beams. For example, requirement of matching the resonance frequency with the ambient dominant frequency is a bottleneck for achieving best performance (Huang and Lin, 2012), and broadband energy harvesting is limited due to the relatively large spacing between resonance frequencies of the first vibrational modes of cantilever beams (Erturk et al., 2009b). Hence, a significant number of studies have focused on the performance improvement of cantilevered beam harvesters and have addressed various designs and configurations to improve their energy harvesting characteristics (Erturk et al., 2009a, 2009b; Ferrari et al., 2008; Friswell and Adhikari, 2010; Huan et al., 2008; Lien and Shu, 2012; Shahruz, 2006; Song et al., 2009). For instance, Lien and Shu (2012) and Lin et al. (2013) investigated the power output performance of multiple cantilevered beam harvesters connected in series and parallel by accounting for interface electronics (e.g. standard, parallel, and series synchronized switch harvesting circuits). Lin et al. (2013) demonstrated that the harvested power output strongly depends on the connection configuration of harvester beams and architecture of interface electronics.

Multiple patch–based energy harvesters (MPBEHs) structurally integrated to thin plates can be conveniently used as an alternative to cantilevered harvester beams which have limited broadband energy harvesting capabilities due to the large spacing between the vibration modes for a given frequency range. Furthermore, in some cases, it might be necessary to use the patch option due to space limitation or to avoid mass loading. Direct attachment of patch-based piezoelectric harvesters to the plate-like structures can reduce the required additional components while enabling more compact energy harvesting mechanisms without modifying the host plate. In addition to these benefits, electrical outputs generated by multiple patches from different vibration modes of thin plates can be combined into a single electrical output, which leads to energy harvesting from all vibration modes of interest.

Thin plate structures are commonly used in aerospace, marine, and automotive systems that can definitely benefit from energy harvesting. However, the literature on piezoelectric patch-based energy harvesting on thin plates is rather limited. Analytical model of a single piezoceramic patch–based harvester has been presented for transverse vibrations of thin plates by Aridogan et al. (2014) and for surface strain fluctuations of high impedance structures by Erturk (2011). Electromechanical finite-element model applicable to patch-based harvesters attached on thin plates was developed by De Marqui et al. (2009), and topology optimization studies for distribution of piezoelectric materials on thin plates were performed by Rupp et al. (2009) and Lee and Youn (2011).

Despite the fact that limited effort has been devoted for piezoelectric patch-based energy harvesting on thin plates, significant literature exists on piezoelectric shunt damping of thin plates. Piezoelectric shunt damping and energy harvesting are associated with dissipation of mechanical energy. While the aim of piezoelectric shunt damping is to attenuate the mechanical energy, piezoelectric energy harvesting is focused on the extraction of usable electrical energy. The method of shunt damping with piezoelectric materials was initially proposed more than 30 years ago by Forward (1979) for vibration suppression. In the early 1990s, analytical formulation of patch-based piezoelectric shunt damping of a thin plate was first presented by Koshigoe and Murdock (1993). Saravanos (1999) presented an analytical model for piezoelectric shunt damping of simply supported multi-layered piezoceramic composite plates. In the subsequent years, several research groups studied design of piezoelectric shunt damping for vibration and noise suppression of thin plates (Behrens et al., 2003; Casadei et al., 2010; Fein, 2008; Kim and Jung, 2006; Kim and Kim, 2004; Manzoni et al., 2012; Moheimani and Behrens, 2004; Niederberger et al., 2004; Richard et al., 2011). However, the energy harvesting capabilities of piezoelectric patches on thin plates (Aridogan et al., 2014; De Marqui et al., 2009; Rupp et al., 2009) have been reported only recently based on analytical (Aridogan et al., 2014) and finite-element (De Marqui et al., 2009; Lee and Youn, 2011; Rupp et al., 2009) modeling.

This article extends the single-patch analytical electroelastic model initially proposed in Aridogan et al. (2014) to series and parallel connections of MPBEHs attached on thin plates for broadband energy harvesting. Coupled electroelastic model of MPBEHs attached on a thin plate is introduced in physical coordinates and transformed into modal coordinates for a fully clamped rectangular (CCCC) plate. Exact steady-state coupled voltage and vibration response expressions are derived for harmonic force excitation by taking into account multiple vibration modes of the plate. Experimental and analytical case studies are then presented for validating the closed-form solutions. Broadband nature of energy harvesting using piezoelectric patches integrated to thin plates is also discussed.

Downloaded from jim.sagepub.com at GEORGIA TECH LIBRARY on September 11, 2014

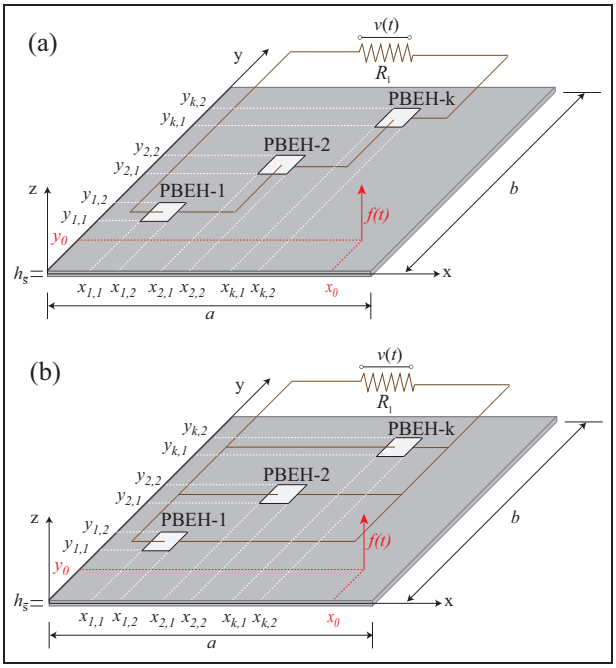

Figure 1. Multiple piezoelectric patch–based energy harvester configurations on a thin plate: (a) series and (b) parallel connections of MPBEHs.
MPBEHs: multiple patch–based energy harvesters.

Distributed-parameter electroelastic modeling

Coupled mechanical equation of a thin plate with MPBEHs

The series and parallel connections of MPBEHs attached on a host plate are shown in Figure 1. MPBEHs are in the form of transversely isotropic and thin piezoceramic patches. The length and the width of the host plate are a and b, respectively. The thickness ($h_{\bar{s}}$) of the plate is assumed to be uniform and much smaller than the total length and width of the plate. In the following, the subscripts $\bar{s}$ and $\bar{p}$ stand for the parameters related to the host structure and MPBEHs, respectively. The number of patch-based harvesters is $n_{\bar{p}}$, and each harvester patch covers a rectangular area with two corners at $(x_{k,1}, y_{k,1})$ and $(x_{k,2}, y_{k,2})$ where $k = 1, 2, \ldots, n_{\bar{p}}$. The thickness of the kth patch is $(h_{\bar{p}})_k$, and each patch is poled in thickness direction (z-axis). The top and bottom faces of the patches are covered by highly conductive and negligibly thin electrode layers. In order to enable the series and parallel connection configurations, surface of the plate is assumed to be electrically insulated, and a load resistance R_l is connected to the resultant terminals of the series and parallel connection configurations of MPBEHs. The plate is persistently excited by transverse point force $f(t)$ at (x_0, y_0), hence the voltage output across the load resistance can be extracted continuously.

The partial differential equation governing the forced vibration of the thin plate with structurally integrated MPBEHs depicted in Figure 1 can be written as (Aridogan et al., 2014)

$$\begin{aligned} & D_{\bar{s}}\left(\frac{\partial^4 w(x,y,t)}{\partial x^4} + 2\frac{\partial^4 w(x,y,t)}{\partial x^2 \partial y^2} + \frac{\partial^4 w(x,y,t)}{\partial y^4}\right) \\ & + c\frac{\partial w(x,y,t)}{\partial t} + \rho_{\bar{s}} h_{\bar{s}} \frac{\partial^2 w(x,y,t)}{\partial t^2} \\ & - \sum_{k=1}^{n_{\bar{p}}} \theta_k v_k(t)\left\{\left[\frac{\mathrm{d}\delta(x-x_{k,1})}{\mathrm{d}x} - \frac{\mathrm{d}\delta(x-x_{k,2})}{\mathrm{d}x}\right]\right. \\ & [H(y-y_{k,1}) - H(y-y_{k,2})] \\ & + \left[\frac{\mathrm{d}\delta(y-y_{k,1})}{\mathrm{d}y} - \frac{\mathrm{d}\delta(y-y_{k,2})}{\mathrm{d}y}\right] \\ & \left.[H(x-x_{k,1}) - H(x-x_{k,2})]\right\} \\ & = f(t)\delta(x-x_0)\delta(y-y_0) \end{aligned} \tag{1}$$

where $w(x, y, t)$ is the transverse deflection of the reference surface (neutral surface) at position (x, y) and time t. The voltage across the electrodes of the kth harvester patch is $v_k(t)$ and the voltage across the resistive load is $v(t)$ as shown in Figure 1(a) and (b). The mass density of the plate is denoted by $\rho_{\bar{s}}$, and the flexural rigidity of the plate is $D_{\bar{s}} = Y_{\bar{s}} h_{\bar{s}}^3/(12 - 12\nu_{\bar{s}}^2)$, where $Y_{\bar{s}}$ and $\nu_{\bar{s}}$ are Young's modulus and Poisson's ratio, respectively. Furthermore, $\delta(x)$ and $\delta(y)$ are the Dirac delta functions, while $H(x)$ and $H(y)$ are the Heaviside functions. The viscous damping coefficient is c and the electromechanical coupling θ_k for the kth harvester patch is

$$\theta_k = (h_{\mathrm{pc}})_k (\bar{e}_{31})_k \tag{2}$$

where $(\bar{e}_{31})_k$ is the effective piezoelectric constant for the kth harvester patch in two-dimensional form as given in Erturk and Inman (2011b) and $(h_{\mathrm{pc}})_k$ is the reference distance (between the neutral surface and the center of the patch thickness) for the kth harvester patch. It should be noted that the piezoceramic patches' inertial and stiffness effects are neglected (by assuming the total amount of piezoelectric material to be much smaller than the host plate dimensions), while the piezoelectrically induced moments are taken into account within equation (1) as a result of the piezoelectric converse effect on the thin plate. In the following, coupled electrical circuit equations are derived for series and parallel configurations. Note that, hereafter, the superscripts s and p stand for the series and parallel connections of MPBEHs.

Coupled electrical circuit equation for series connection

The series configuration of MPBEHs to a load resistance R_l is represented by a simple electrical circuit in

Downloaded from jim.sagepub.com at GEORGIA TECH LIBRARY on September 11, 2014

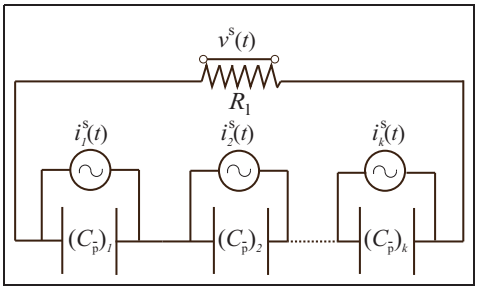

Figure 2. Electrical circuit for series connection of MPBEHs to a resistive load (current sources depend on the voltage output due to backward coupling).
MPBEHs: multiple patch–based energy harvesters.

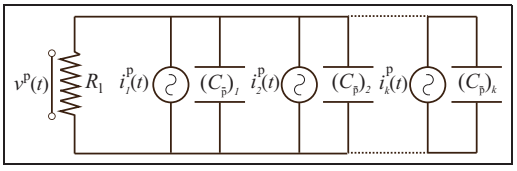

Figure 3. Electrical circuit for parallel connection of MPBEHs to a resistive load (current sources depend on the voltage output due to backward coupling).
MPBEHs: multiple patch–based energy harvesters.

Figure 2. Each harvester patch is represented as a dependent current source $i_k^s(t)$ in parallel with its internal capacitance $(C_{\bar{p}})_k$.

The governing electrical circuit equation for each harvester patch can be obtained as

$$(C_{\bar{p}})_k \frac{dv_k^s(t)}{dt} + \frac{1}{R_l} v^s(t) = i_k^s(t) \quad k = 1, 2, \ldots, n_{\bar{p}} \tag{3}$$

where $v_k^s(t)$ is the voltage across the electrodes of the kth harvester patch and $v^s(t)$ is the voltage across the resistive load. The number of governing circuit equations is equal to the number of harvester patches ($n_{\bar{p}}$). The internal capacitance of the kth harvester patch $(C_{\bar{p}})_k$ can be expressed as

$$(C_{\bar{p}})_k = (\bar{\varepsilon}_{33}^S)_k \frac{(l_{\bar{p}})_k (w_{\bar{p}})_k}{(h_{\bar{p}})_k} \tag{4}$$

where the length, width, and thickness of the kth harvester patch are $(l_{\bar{p}})$, $(w_{\bar{p}})_k$, and $(h_{\bar{p}})_k$, respectively, and $(\bar{\varepsilon}_{33}^S)_k$ is the permittivity of the kth patch at constant strain. The current produced by the kth harvester patch can be obtained as (Aridogan et al., 2014)

$$i_k^s(t) = -\theta_k \int_{y_{k,1}}^{y_{k,2}} \int_{x_{k,1}}^{x_{k,2}} \left[\frac{\partial^3 w(x,y,t)}{\partial x^2 \partial t} + \frac{\partial^3 w(x,y,t)}{\partial y^2 \partial t} \right] dx dy \tag{5}$$

which clearly depends on the rate of change of strain distribution on the plate's surface covered by the harvester patch. The area integral of the time derivative of strain distribution determines the collected charge output on the electrode layer of the harvester patch. Therefore, depending on the location of the harvester patches on the thin plate, charge cancellations may occur. The reader is referred to Aridogan et al. (2014) for detailed discussions regarding the relationship between the strain distribution and the power output of a single patch–based harvester attached on a thin plate. It should be noted that the electrical outputs of multiple patches are combined in the cases of series and parallel connections; consequently, enhancement or cancellation of the electrical output can take place. Therefore, the relative positioning of the harvester patches and proper combination of their terminals are also important.

The distributed-parameter electroelastic model of MPBEHs combined in series configuration consists of a mechanical equation (equation (1)) and $n_{\bar{p}}$ number of electrical circuit equations (equation (3)). Once these electromechanically coupled $n_{\bar{p}} + 1$ number of equations are simultaneously solved for a given force input, vibration response of the plate and voltage output of each harvester patch can be calculated. Then, the voltage output across the resistor is calculated using

$$v^s(t) = \sum_{k=1}^{n_{\bar{p}}} v_k^s(t) \tag{6}$$

Coupled electrical circuit equation for parallel connection

The electrical circuit in Figure 3 illustrates the coupled electrical dynamics of harvester patches combined in parallel. The harvester patches are all connected in parallel to a resistor, and each harvester patch is again modeled as a dependent current source with a parallel internal capacitance. Note that in the parallel connection configuration, the voltage across the electrodes of each harvester patch $v_k^p(t)$ is equal to the voltage $v^p(t)$ across the resistor.

The governing electrical equation for MPBEHs connected in parallel can be obtained as

$$\frac{dv^p(t)}{dt} \sum_{k=1}^{n_{\bar{p}}} (C_{\bar{p}})_k + \frac{v^p(t)}{R_l} = \sum_{k=1}^{n_{\bar{p}}} i_k^p(t) \tag{7}$$

where the capacitance and the current output of the kth harvester are $(C_{\bar{p}})_k$ and $i_k^p(t)$, which are identical to equations (4) and (5), respectively. Thus, one circuit equation governs the electrical part of the electroelastic model of MPBEHs connected in parallel. Therefore, two differential equations (mechanical part in equation (1) and electrical part in equation (7)) form the electroelastic model of parallel-connected harvester patches

Downloaded from jim.sagepub.com at GEORGIA TECH LIBRARY on September 11, 2014

attached on a thin plate. For a given force input, voltage across the load resistance and shunted vibration response of the plate can be calculated by solving these two electromechanically coupled differential equations simultaneously.

Electroelastic equations in modal coordinates

Modal analysis of a thin plate

The vibration response of a fully clamped thin plate can be represented as

$$w^{\mathrm{s}}(x,y,t) = \sum_{n=1}^{\infty}\sum_{m=1}^{\infty} \phi_{mn}(x,y)\eta^{\mathrm{s}}_{mn}(t) \tag{8a}$$

$$w^{\mathrm{p}}(x,y,t) = \sum_{n=1}^{\infty}\sum_{m=1}^{\infty} \phi_{mn}(x,y)\eta^{\mathrm{p}}_{mn}(t) \tag{8b}$$

where $\phi_{mn}(x,y)$ is the mass-normalized eigenfunction of the mnth vibration mode in x- and y-axes, and $\eta^{\mathrm{s}}_{mn}(t)$ and $\eta^{\mathrm{p}}_{mn}(t)$ are the generalized modal mechanical coordinates for the series and parallel connections of harvester patches, respectively.

The fully clamped boundary conditions of a thin rectangular plate ensure zero deflections and zero slopes along all four edges. For the series connection of harvester patches, boundary conditions of a CCCC plate with a length of a and a width of b can be written as

$$w^{\mathrm{s}}(0,y,t)=0 \quad w^{\mathrm{s}}(a,y,t)=0 \quad w^{\mathrm{s}}(x,0,t)=0 \quad w^{\mathrm{s}}(x,b,t)=0$$
$$\left.\frac{\partial w^{\mathrm{s}}(x,y,t)}{\partial x}\right|_{x=0}=0 \quad \left.\frac{\partial w^{\mathrm{s}}(x,y,t)}{\partial x}\right|_{x=a}=0 \quad \left.\frac{\partial w^{\mathrm{s}}(x,y,t)}{\partial \mathrm{y}}\right|_{y=0}=0 \quad \left.\frac{\partial w^{\mathrm{s}}(x,y,t)}{\partial \mathrm{y}}\right|_{y=b}=0 \tag{9}$$

and expectedly, the boundary conditions are the same in parallel connection. The eigenfunctions satisfying the boundary conditions of a CCCC plate can be derived by using the separation of spatial variables (Xing and Liu, 2009) as follows

$$\phi_{mn}(x,y) = \Theta_{mn}\left(\cos\lambda^x_{mn}x - \sigma^x_{mn}\sin\lambda^x_{mn}x - \cos\,h\mu^x_{mn}x + \frac{\lambda^x_{mn}}{\mu^x_{mn}}\sigma^x_{mn}\sin\,h\mu^x_{mn}x\right) \times\left(\cos\lambda^y_{mn}y - \sigma^y_{mn}\sin\lambda^y_{mn}y - \cos\,h\mu^y_{mn}y + \frac{\lambda^y_{mn}}{\mu^y_{mn}}\sigma^y_{mn}\sin\,h\mu^y_{mn}y\right) \tag{10}$$

where σ^x_{mn} and σ^y_{mn} are

$$\sigma^x_{mn} = \frac{\cos\lambda^x_{mn}a - \cos\,h\mu^x_{mn}a}{\sin\lambda^x_{mn}a - \frac{\lambda^x_{mn}}{\mu^x_{mn}}\sin\,h\mu^x_{mn}a}$$
$$\sigma^y_{mn} = \frac{\cos\lambda^y_{mn}b - \cos\,h\mu^y_{mn}b}{\sin\lambda^y_{mn}b - \frac{\lambda^y_{mn}}{\mu^y_{mn}}\sin\,h\mu^y_{mn}b} \tag{11}$$

and the modal amplitude constant Θ_{mn} can be calculated by applying the following orthogonality conditions

$$\int_0^b\int_0^a \rho_{\bar{\mathrm{s}}}h_{\bar{\mathrm{s}}}\,\phi_{mn}(x,y)\,\phi_{rs}(x,y)\,\mathrm{d}x\,\mathrm{d}y = \delta_{mr}\delta_{ns} \tag{12a}$$

$$\int_0^b\int_0^a D_{\bar{\mathrm{s}}}\left(\frac{\partial^2\phi_{mn}(x,y)}{\partial x^2}\frac{\partial^2\phi_{rs}(x,y)}{\partial x^2} + 2\frac{\partial^2\phi_{mn}(x,y)}{\partial x^2}\frac{\partial^2\phi_{rs}(x,y)}{\partial y^2} + \frac{\partial^2\phi_{mn}(x,y)}{\partial y^2}\frac{\partial^2\phi_{rs}(x,y)}{\partial y^2}\right)\mathrm{d}x\mathrm{d}y = \omega^2_{mn}\delta_{mr}\delta_{ns} \tag{12b}$$

where δ_{mr} and δ_{ns} are Kronecker delta functions; δ_{mr} equals to unity when $m=r$ and it is zero when $m\neq r$; similarly, δ_{ns} equals to unity only for $n=s$ and zero for $n\neq s$. The undamped natural frequency ω_{mn} for the mnth vibration mode of the plate in short-circuit conditions (as $R_l\to 0$) is given by

$$\omega_{mn} = \sqrt{\frac{\kappa^4_{mn}}{\rho_{\bar{\mathrm{s}}}h_{\bar{\mathrm{s}}}}D_{\bar{\mathrm{s}}}} \tag{13}$$

where κ_{mn} is the frequency parameter of the undamped plate, and the eigenvalues (λ^x_{mn}, λ^y_{mn}, μ^x_{mn}, μ^y_{mn}) can be calculated in the intervals of

$$\lambda^x_{mn}a \in \left[m\pi, m\pi + \frac{\pi}{2}\right], \quad m=1,2,\ldots$$
$$\lambda^y_{mn}b \in \left[n\pi, n\pi + \frac{\pi}{2}\right], \quad n=1,2,\ldots \tag{14}$$

by using a transcendental solver for the algebraic equations, which are presented in equations (15a) to (15e) as follows (Xing and Liu, 2009)

$$\frac{1-\cos\,h\mu^x_{mn}a\,\cos\lambda^x_{mn}a}{\sin\,h\mu^x_{mn}a\,\sin\lambda^x_{mn}a} = \frac{(\lambda^x_{mn})^2-(\mu^x_{mn})^2}{2\lambda^x_{mn}\mu^x_{mn}} \tag{15a}$$

$$\frac{1-\cos\,h\mu^y_{mn}b\,\cos\lambda^y_{mn}b}{\sin\,\mathrm{h}\mu^y_{mn}b\,\sin\lambda^y_{mn}b} = \frac{(\lambda^y_{mn})^2-(\mu^y_{mn})^2}{2\lambda^y_{mn}\mu^y_{mn}} \tag{15b}$$

$$\kappa_{mn} = \sqrt{(\lambda^x_{mn})^2+(\lambda^y_{mn})^2} \tag{15c}$$

$$\mu^y_{mn} = \sqrt{2\kappa^2_{mn}-(\lambda^y_{mn})^2} \tag{15d}$$

Downloaded from jim.sagepub.com at GEORGIA TECH LIBRARY on September 11, 2014

$$\mu_{mn}^{x} = \sqrt{2\kappa_{mn}^{2} - (\lambda_{mn}^{x})^{2}} \tag{15e}$$

These modal parameters (eigenvalues and eigenfunctions) are derived for the short-circuit condition ($R_l \to 0$) of series and parallel connections of harvester patches since the voltage term in the mechanical part of the electroelastic model in equation (1) becomes zero ($v_k \to 0$) in short-circuit condition. Therefore, the electromechanical coupling between the harvester patches and the plate vanishes in short-circuit conditions, and standard modal analysis is valid. For finite load resistance values, the electromechanical coupling between the harvester patches and the plate takes place due to the induced moments created along the edges of the harvester patch. In this case, modal mechanical response of the plate depends on the voltage of each harvester patch and differs in series and parallel configurations of harvester patches. In the following sections, differential equations governing the modal mechanical responses of the series and parallel connections are obtained by transforming the coupled mechanical and electrical equations of MPBEHs into modal coordinates.

Modal transformation of coupled equations for series connection

The mechanical equation of motion given by equation (1) in the physical coordinates can be transformed into modal coordinates by following the modal analysis process (Aridogan et al., 2014). This procedure includes substituting equation (8a) into equation (1) and applying the orthogonality conditions given by equations (12a) and (12b), yielding

$$\begin{aligned}\frac{\mathrm{d}^2\eta_{mn}^{\mathrm{s}}(t)}{\mathrm{d}t^2} + 2\zeta_{mn}\omega_{mn}\frac{\mathrm{d}\eta_{mn}^{\mathrm{s}}(t)}{\mathrm{d}t} + \omega_{mn}^2\eta_{mn}^{\mathrm{s}}(t) \\ - \sum_{k=1}^{n_{\bar{\mathrm{p}}}} (\tilde{\theta}_{mn})_k v_k^{\mathrm{s}}(t) = f_{mn}(t)\end{aligned} \tag{16}$$

where ω_{mn} is the undamped natural frequency (in short-circuit condition) and ζ_{mn} is the modal damping ratio for the mnth vibration mode of the thin plate. Note that the modal damping ratio can be obtained by using the standard damping identification techniques (Erturk and Inman, 2011a) based on experimental measurements. The transverse force in modal coordinates $f_{mn}(t)$ is

$$f_{mn}(t) = f(t)\phi_{mn}(x_0, y_0) \tag{17}$$

and the electromechanical coupling term for the kth harvester in modal coordinates is given by

$$(\tilde{\theta}_{mn})_k = \theta_k \int_{y_{k,1}}^{y_{k,2}} \int_{x_{k,1}}^{x_{k,2}} \left[\frac{\partial^2\phi_{mn}(x,y)}{\partial x^2} + \frac{\partial^2\phi_{mn}(x,y)}{\partial y^2}\right] \mathrm{d}x\mathrm{d}y \tag{18}$$

To obtain the electrical circuit equation of the electroelastic model in modal coordinates, first, equation (8a) is substituted into the current output expression in equation (5) to give

$$\begin{aligned}i_k^{\mathrm{s}}(t) = -\theta_k \sum_{n=1}^{\infty}\sum_{m=1}^{\infty} \int_{y_{k,1}}^{y_{k,2}} \int_{x_{k,1}}^{x_{k,2}} \left[\frac{\partial^2\phi_{mn}(x,y)}{\partial x^2} + \frac{\partial^2\phi_{mn}(x,y)}{\partial y^2}\right] \\ \frac{\mathrm{d}\eta_{mn}^{\mathrm{s}}(t)}{\mathrm{d}t}\mathrm{d}x\mathrm{d}y\end{aligned} \tag{19}$$

and then equation (19) can be reduced to

$$i_k^{\mathrm{s}}(t) = -\sum_{n=1}^{\infty}\sum_{m=1}^{\infty} (\tilde{\theta}_{mn})_k \frac{\mathrm{d}\eta_{mn}^{\mathrm{s}}(t)}{\mathrm{d}t} \tag{20}$$

by substituting electromechanical coupling term given by equation (18) into equation (19). Then, using equations (20) and (3), the electrical part of the electroelastic model can be obtained as

$$\begin{aligned}\sum_{n=1}^{\infty}\sum_{m=1}^{\infty} (\tilde{\theta}_{mn})_k \frac{\mathrm{d}\eta_{mn}^{\mathrm{s}}(t)}{\mathrm{d}t} + (C_{\bar{\mathrm{p}}})_k \frac{\mathrm{d}v_k^{\mathrm{s}}(t)}{\mathrm{d}t} \\ + \frac{1}{R_l}\sum_{k=1}^{n_{\bar{\mathrm{p}}}} v_k^{\mathrm{s}}(t) = 0 \quad \text{where } k = 1, 2, \ldots, n_{\bar{\mathrm{p}}}\end{aligned} \tag{21}$$

here, $n_{\bar{\mathrm{p}}}$ number of equations in modal coordinates constitute the electrical part of the electroelastic model. As a result, the distributed-parameter electroelastic model of the harvester patches connected in series is expressed in modal coordinates by $n_{\bar{\mathrm{p}}} + 1$ number of ordinary differential equations given by equations (16) and (21).

Modal transformation of coupled equations for parallel connection

The electromechanically coupled equation of motion can be obtained in modal coordinates as

$$\begin{aligned}\frac{\mathrm{d}^2\eta_{mn}^{\mathrm{p}}(t)}{\mathrm{d}t^2} + 2\zeta_{mn}\omega_{mn}\frac{\mathrm{d}\eta_{mn}^{\mathrm{p}}(t)}{\mathrm{d}t} + \omega_{mn}^2\eta_{mn}^{\mathrm{p}}(t) \\ - v^{\mathrm{p}}(t)\sum_{k=1}^{n_{\bar{\mathrm{p}}}} (\tilde{\theta}_{mn})_k = f_{mn}(t)\end{aligned} \tag{22}$$

For the electrical part of the electroelastic model, equation (8b) can be substituted into equation (5) to obtain

$$\begin{aligned}i_k^{\mathrm{p}}(t) = -\theta_k \sum_{n=1}^{\infty}\sum_{m=1}^{\infty} \int_{y_{k,1}}^{y_{k,2}} \int_{x_{k,1}}^{x_{k,2}} \left[\frac{\partial^2\phi_{mn}(x,y)}{\partial x^2} + \frac{\partial^2\phi_{mn}(x,y)}{\partial y^2}\right] \\ \frac{\mathrm{d}\eta_{mn}^{\mathrm{p}}(t)}{\mathrm{d}t}\mathrm{d}x\mathrm{d}y\end{aligned} \tag{23}$$

Equation (23) is then simplified to

Downloaded from jim.sagepub.com at GEORGIA TECH LIBRARY on September 11, 2014

$$i_k^{\mathrm{p}}(t) = -\sum_{n=1}^{\infty}\sum_{m=1}^{\infty}(\tilde{\theta}_{mn})_k \frac{\mathrm{d}\eta_{mn}^{\mathrm{p}}(t)}{\mathrm{d}t} \tag{24}$$

by using the electromechanical coupling term $(\tilde{\theta}_{mn})_k$ given by equation (18). Then, substitution of equation (24) into equation (7) gives the electrical part in modal coordinates as

$$\sum_{k=1}^{n_{\bar{\mathrm{p}}}}\sum_{n=1}^{\infty}\sum_{m=1}^{\infty}(\tilde{\theta}_{mn})_k \frac{\mathrm{d}\eta_{mn}^{\mathrm{p}}(t)}{\mathrm{d}t} + \frac{\mathrm{d}v^{\mathrm{p}}(t)}{\mathrm{d}t}\sum_{k=1}^{n_{\bar{\mathrm{p}}}}(C_{\bar{\mathrm{p}}})_k + \frac{v^{\mathrm{p}}(t)}{R_l} = 0 \tag{25}$$

Consequently, the distributed-parameter electroelastic model for the parallel configuration of harvester patches in modal coordinates consists of two differential equations as given by equations (22) and (25).

Steady-state response to harmonic force excitation

Multimode electroelastic frequency response functions for series connection

The coupled electroelastic equations forming the distributed-parameter model of series-connected harvester patches in modal coordinates are given by equations (16) and (21). If the transverse point force acting on the surface of the plate is assumed to be harmonic of the form $f(t) = F_0 e^{\mathrm{j}\omega t}$ (where F_0 is the amplitude of the force and ω is the excitation frequency), the mechanical and electrical responses are assumed to be harmonic based on the linear system assumption as follows

$$\eta_{mn}^{\mathrm{s}}(t) = \eta_{mn}^{\mathrm{s}} e^{\mathrm{j}\omega t}, \quad v_k^{\mathrm{s}}(t) = V_k^{\mathrm{s}} e^{\mathrm{j}\omega t} \tag{26}$$

where η_{mn}^{s} and V_k^{s} are complex valued. The coupled mechanical and electrical equations of the distributed-parameter model for series configuration then yield the following forms

$$(\omega_{mn}^2 - \omega^2 + \mathrm{j}2\zeta_{mn}\omega_{mn}\omega)\eta_{mn}^{\mathrm{s}} - \sum_{k=1}^{n_{\bar{\mathrm{p}}}}(\tilde{\theta}_{mn})_k V_k^s = F_0\phi_{mn}(x_0, y_0) \tag{27}$$

and

$$\mathrm{j}\omega\sum_{n=1}^{\infty}\sum_{m=1}^{\infty}(\tilde{\theta}_{mn})_k\eta_{mn}^{\mathrm{s}} + \mathrm{j}\omega(C_{\bar{\mathrm{p}}})_k V_k^s + \frac{1}{R_l}\sum_{k=1}^{n_{\bar{\mathrm{p}}}}V_k^s = 0 \quad \text{where } k = 1, 2, \ldots, n_{\bar{\mathrm{p}}} \tag{28}$$

Then, the complex amplitude η_{mn}^{s} can be extracted from equation (27) as

$$\eta_{mn}^{\mathrm{s}} = \frac{F_0\phi_{mn}(x_0, y_0) + \boldsymbol{\theta}_{mn}^T\mathbf{V}^{\mathrm{s}}}{\omega_{mn}^2 - \omega^2 + \mathrm{j}2\zeta_{mn}\omega_{mn}\omega} \tag{29}$$

here, the voltage amplitude vector $\mathbf{V}^{\mathrm{s}}$ with the dimensions of $n_{\bar{\mathrm{p}}} \times 1$ includes the voltage amplitude of each harvester patch as $\mathbf{V}^{\mathrm{s}} = [V_1^{\mathrm{s}} \;\; V_2^{\mathrm{s}} \;\; \cdots \;\; V_{n_{\bar{\mathrm{p}}}}^{\mathrm{s}}]^T$, where superscript T stands for the transpose, and the electromechanical coupling vector $\boldsymbol{\theta}_{mn}$ with the dimensions of $n_{\bar{\mathrm{p}}} \times 1$ is $\boldsymbol{\theta}_{mn} = [(\tilde{\theta}_{mn})_1 \;\; (\tilde{\theta}_{mn})_2 \;\; \cdots \;\; (\tilde{\theta}_{mn})_{n_{\bar{\mathrm{p}}}}]^T$.

The voltage amplitude vector $\mathbf{V}^{\mathrm{s}}$ can be solved using the following matrix form

$$\mathbf{V}^{\mathrm{s}} = F_0\mathbf{Q}^{-1}\mathbf{P} \tag{30}$$

where $\mathbf{Q}$ is a square matrix with the dimensions of $n_{\bar{\mathrm{p}}} \times n_{\bar{\mathrm{p}}}$ and $\mathbf{P}$ is a column vector with the dimensions of $n_{\bar{\mathrm{p}}} \times 1$, which can be written as

$$\mathbf{Q} = \begin{bmatrix} \frac{1 + \mathrm{j}\omega(C_{\bar{\mathrm{p}}})_1 R_l}{R_l} + \sum_{n=1}^{\infty}\sum_{m=1}^{\infty}\frac{\mathrm{j}\omega\left[(\tilde{\theta}_{mn})_1\right]^2}{\omega_{mn}^2 - \omega^2 + \mathrm{j}2\zeta_{mn}\omega_{mn}\omega} & \cdots & \cdots & \frac{1}{R_l} + \sum_{n=1}^{\infty}\sum_{m=1}^{\infty}\frac{\mathrm{j}\omega(\tilde{\theta}_{mn})_1(\tilde{\theta}_{mn})_{n_{\bar{\mathrm{p}}}}}{\omega_{mn}^2 - \omega^2 + \mathrm{j}2\zeta_{mn}\omega_{mn}\omega} \\ \vdots & \ddots & & \vdots \\ \vdots & & \ddots & \vdots \\ \frac{1}{R_l} + \sum_{n=1}^{\infty}\sum_{m=1}^{\infty}\frac{\mathrm{j}\omega(\tilde{\theta}_{mn})_{n_{\bar{\mathrm{p}}}}(\tilde{\theta}_{mn})_1}{\omega_{mn}^2 - \omega^2 + \mathrm{j}2\zeta_{mn}\omega_{mn}\omega} & \cdots & \cdots & \frac{1 + \mathrm{j}\omega(C_{\bar{\mathrm{p}}})_{n_{\bar{\mathrm{p}}}} R_l}{R_l} + \sum_{n=1}^{\infty}\sum_{m=1}^{\infty}\frac{\mathrm{j}\omega\left[(\tilde{\theta}_{mn})_{n_{\bar{\mathrm{p}}}}\right]^2}{\omega_{mn}^2 - \omega^2 + \mathrm{j}2\zeta_{mn}\omega_{mn}\omega} \end{bmatrix} \tag{31}$$

$$\mathbf{P} = \begin{bmatrix} -\sum_{n=1}^{\infty}\sum_{m=1}^{\infty}\frac{\mathrm{j}\omega(\tilde{\theta}_{mn})_1\phi_{mn}(x_0, y_0)}{\omega_{mn}^2 - \omega^2 + \mathrm{j}2\zeta_{mn}\omega_{mn}\omega} \\ \vdots \\ \vdots \\ -\sum_{n=1}^{\infty}\sum_{m=1}^{\infty}\frac{\mathrm{j}\omega(\tilde{\theta}_{mn})_{n_{\bar{\mathrm{p}}}}\phi_{mn}(x_0, y_0)}{\omega_{mn}^2 - \omega^2 + \mathrm{j}2\zeta_{mn}\omega_{mn}\omega} \end{bmatrix}$$

Downloaded from jim.sagepub.com at GEORGIA TECH LIBRARY on September 11, 2014

Therefore, the steady-state voltage output $v^{\mathrm{s}}(t)$ across the resistive load can be obtained as

$$v^{\mathrm{s}}(t) = \sum_{k=1}^{n_{\bar{\mathrm{p}}}} V_k^{\mathrm{s}} e^{\mathrm{j}\omega t} = \mathbf{u}^T F_0 \mathbf{Q}^{-1} \mathbf{P} e^{\mathrm{j}\omega t} \tag{32}$$

where $\mathbf{u}$ is a unit vector with the dimensions of $n_{\bar{\mathrm{p}}} \times 1$.

The steady-state vibration response can be written as

$$w^{\mathrm{s}}(x,y,t) = \sum_{n=1}^{\infty}\sum_{m=1}^{\infty} \Phi_{mn}(x,y) \frac{F_0\phi_{mn}(x_0,y_0) + \boldsymbol{\theta}_{mn}^T F_0 \mathbf{Q}^{-1}\mathbf{P}}{\omega_{mn}^2 - \omega^2 + \mathrm{j}2\zeta_{mn}\omega_{mn}\omega} e^{\mathrm{j}\omega t} \tag{33}$$

After formulating the steady-state responses, two multi-mode frequency response functions (FRFs) can be extracted between two outputs and one input: voltage output-to-force input ratio (i.e. voltage FRF $\alpha^{\mathrm{s}}(\omega)$) and the displacement-to-force input ratio (i.e. displacement FRF $\beta^{\mathrm{s}}(x,y,\omega)$). The voltage FRF is given by

$$\alpha^{\mathrm{s}}(\omega) = \frac{v^{\mathrm{s}}(t)}{F_0 e^{\mathrm{j}\omega t}} = \mathbf{u}^T \mathbf{Q}^{-1}\mathbf{P} \tag{34}$$

Similarly, the displacement FRF at positions x and y on the plate is

$$\beta^{\mathrm{s}}(x,y,\omega) = \frac{w^{\mathrm{s}}(x,y,t)}{F_0 e^{\mathrm{j}\omega t}} = \sum_{n=1}^{\infty}\sum_{m=1}^{\infty} \phi_{mn}(x,y) \frac{\phi_{mn}(x_0,y_0) + \boldsymbol{\theta}_{mn}^T \mathbf{Q}^{-1}\mathbf{P}}{\omega_{mn}^2 - \omega^2 + \mathrm{j}2\zeta_{mn}\omega_{mn}\omega} \tag{35}$$

Multimode electroelastic FRFs for parallel connection

Similar to the series connection case, when the transverse point force acting on the surface of the plate is assumed to be harmonic of the form $f(t) = F_0 e^{\mathrm{j}\omega t}$, the steady-state mechanical and electrical responses are

$$\eta_{mn}^{\mathrm{p}}(t) = \mathrm{H}_{mn}^{\mathrm{p}} e^{\mathrm{j}\omega t}, \quad v^{\mathrm{p}}(t) = V^{\mathrm{p}} e^{\mathrm{j}\omega t} \tag{36}$$

where $\mathrm{H}_{mn}^{\mathrm{p}}$ and V^{p} are complex valued amplitudes. Recall that in the parallel connection case, the voltage output of each harvester patch is equal to the voltage $v^{\mathrm{p}}(t)$ across the resistor (see Figure 3). Using the harmonic forms of steady-state structural and electrical responses in equation (36), the coupled mechanical and electrical equations for parallel configuration can be written as

$$(\omega_{mn}^2 - \omega^2 + \mathrm{j}2\zeta_{mn}\omega_{mn}\omega)\mathrm{H}_{mn}^{\mathrm{p}} - V^{\mathrm{p}} \sum_{k=1}^{n_{\bar{\mathrm{p}}}} (\tilde{\theta}_{mn})_k = F_0\phi_{mn}(x_0,y_0) \tag{37}$$

and

$$\sum_{k=1}^{n_{\bar{\mathrm{p}}}}\sum_{n=1}^{\infty}\sum_{m=1}^{\infty} \mathrm{j}\omega(\tilde{\theta}_{mn})_k \eta_{mn}^{\mathrm{p}} + \left(\sum_{k=1}^{n_{\bar{\mathrm{p}}}} \mathrm{j}\omega(C_{\bar{\mathrm{p}}})_k + \frac{1}{R_l}\right) V^{\mathrm{p}} = 0 \tag{38}$$

Then, the complex amplitude η_{mn}^{p} can be extracted from equation (37) as

$$\eta_{mn}^{\mathrm{p}} = \frac{F_0\phi_{mn}(x_0,y_0) + V^{\mathrm{p}} \sum_{k=1}^{n_{\bar{\mathrm{p}}}} (\tilde{\theta}_{mn})_k}{\omega_{mn}^2 - \omega^2 + \mathrm{j}2\zeta_{mn}\omega_{mn}\omega} \tag{39}$$

and substituting equation (39) into equation (38) gives the steady-state voltage $v^{\mathrm{p}}(t)$ across the resistor as

$$v^{\mathrm{p}}(t) = V^{\mathrm{p}} e^{\mathrm{j}\omega t} = \frac{-\sum_{k=1}^{n_{\bar{\mathrm{p}}}}\sum_{n=1}^{\infty}\sum_{m=1}^{\infty} \frac{\mathrm{j}\omega(\tilde{\theta}_{mn})_k F_0\phi_{mn}(x_0,y_0)}{\omega_{mn}^2 - \omega^2 + \mathrm{j}2\zeta_{mn}\omega_{mn}\omega}}{\mathrm{j}\omega \sum_{k=1}^{n_{\bar{\mathrm{p}}}} (C_{\bar{\mathrm{p}}})_k + \frac{1}{R_l} + \sum_{k=1}^{n_{\bar{\mathrm{p}}}}\sum_{n=1}^{\infty}\sum_{m=1}^{\infty} \frac{\mathrm{j}\omega(\tilde{\theta}_{mn})_k \sum_{k=1}^{n_{\bar{\mathrm{p}}}} (\tilde{\theta}_{mn})_k}{\omega_{mn}^2 - \omega^2 + \mathrm{j}2\zeta_{mn}\omega_{mn}\omega}} e^{\mathrm{j}\omega t} \tag{40}$$

and the transverse deflection of the plate at any point (x,y) and time t can be obtained by using equations (8b), (36), (39), and (40) as follows

$$w^{\mathrm{p}}(x,y,t) = \sum_{n=1}^{\infty}\sum_{m=1}^{\infty} \frac{\phi_{mn}(x,y)}{\omega_{mn}^2 - \omega^2 + \mathrm{j}2\zeta_{mn}\omega_{mn}\omega} \left\{ F_0\phi_{mn}(x_0,y_0) - \frac{\left[\sum_{k=1}^{n_{\bar{\mathrm{p}}}}\sum_{n=1}^{\infty}\sum_{m=1}^{\infty} \frac{\mathrm{j}\omega(\tilde{\theta}_{mn})_k F_0\phi_{mn}(x_0,y_0)}{\omega_{mn}^2 - \omega^2 + \mathrm{j}2\zeta_{mn}\omega_{mn}\omega}\right] \times \sum_{k=1}^{n_{\bar{\mathrm{p}}}} (\tilde{\theta}_{mn})_k}{\mathrm{j}\omega \sum_{k=1}^{n_{\bar{\mathrm{p}}}} (C_{\bar{\mathrm{p}}})_k + \frac{1}{R_l} + \sum_{k=1}^{n_{\bar{\mathrm{p}}}}\sum_{n=1}^{\infty}\sum_{m=1}^{\infty} \frac{\mathrm{j}\omega(\tilde{\theta}_{mn})_k \sum_{k=1}^{n_{\bar{\mathrm{p}}}} (\tilde{\theta}_{mn})_k}{\omega_{mn}^2 - \omega^2 + \mathrm{j}2\zeta_{mn}\omega_{mn}\omega}} \right\} e^{\mathrm{j}\omega t} \tag{41}$$

The closed-form expression for the voltage FRF $\alpha^{\mathrm{p}}(\omega)$ is given by

Downloaded from jim.sagepub.com at GEORGIA TECH LIBRARY on September 11, 2014

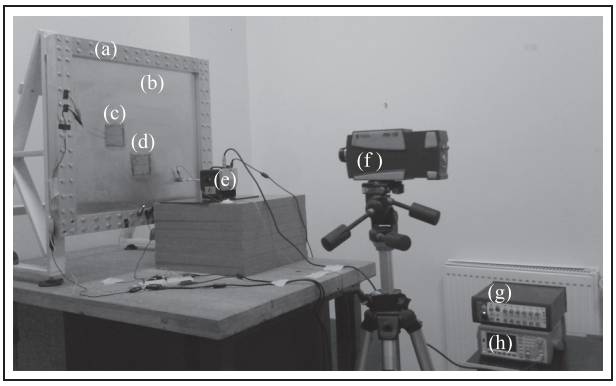

Figure 4. Experimental setup: (a) clamping frames, (b) aluminum plate, (c) PBEH-1, (d) PBEH-2, (e) shaker with a force transducer, (f) laser vibrometer, (g) data acquisition unit, and (h) signal generator.

$$\alpha^{\mathrm{p}}(\omega) = \frac{v^{\mathrm{p}}(t)}{F_0 e^{\mathrm{j}\omega t}} = \frac{-\sum_{k=1}^{n_{\tilde{\mathrm{p}}}}\sum_{n=1}^{\infty}\sum_{m=1}^{\infty}\frac{\mathrm{j}\omega(\tilde{\theta}_{mn})_k\phi_{mn}(x_0,y_0)}{\omega_{mn}^2-\omega^2+\mathrm{j}2\zeta_{mn}\omega_{mn}\omega}}{\mathrm{j}\omega\sum_{k=1}^{n_{\tilde{\mathrm{p}}}}(C_{\tilde{\mathrm{p}}})_k+\frac{1}{R_l}+\sum_{k=1}^{n_{\tilde{\mathrm{p}}}}\sum_{n=1}^{\infty}\sum_{m=1}^{\infty}\frac{\mathrm{j}\omega(\tilde{\theta}_{mn})_k\sum_{k=1}^{n_{\tilde{\mathrm{p}}}}(\tilde{\theta}_{mn})_k}{\omega_{mn}^2-\omega^2+\mathrm{j}2\zeta_{mn}\omega_{mn}\omega}} \quad (42)$$

and the displacement FRF $\beta^{\mathrm{p}}(x,y,\omega)$ is

$$\beta^{\mathrm{p}}(x,y,\omega) = \sum_{n=1}^{\infty}\sum_{m=1}^{\infty}\frac{\phi_{mn}(x,y)}{\omega_{mn}^2-\omega^2+\mathrm{j}2\zeta_{mn}\omega_{mn}\omega}\left\{\phi_{mn}(x_0,y_0)-\frac{\left[\sum_{k=1}^{n_{\tilde{\mathrm{p}}}}\sum_{n=1}^{\infty}\sum_{m=1}^{\infty}\frac{\mathrm{j}\omega(\tilde{\theta}_{mn})_k\phi_{mn}(x_0,y_0)}{\omega_{mn}^2-\omega^2+\mathrm{j}2\zeta_{mn}\omega_{mn}\omega}\right]\times\sum_{k=1}^{n_{\tilde{\mathrm{p}}}}(\tilde{\theta}_{mn})_k}{\mathrm{j}\omega\sum_{k=1}^{n_{\tilde{\mathrm{p}}}}(C_{\tilde{\mathrm{p}}})_k+\frac{1}{R_l}+\sum_{k=1}^{n_{\tilde{\mathrm{p}}}}\sum_{n=1}^{\infty}\sum_{m=1}^{\infty}\frac{\mathrm{j}\omega(\tilde{\theta}_{mn})_k\sum_{k=1}^{n_{\tilde{\mathrm{p}}}}(\tilde{\theta}_{mn})_k}{\omega_{mn}^2-\omega^2+\mathrm{j}2\zeta_{mn}\omega_{mn}\omega}}\right\} \quad (43)$$

Note that these multi-mode expressions can be used for thin plates with different boundary conditions using the respective modal parameters (natural frequencies and mass-normalized mode shapes).

Experimental validations

Experimental setup

The experimental setup used for model validation and experimental demonstrations is shown in Figure 4. A rectangular aluminum sheet plate is used as a thin host plate, and all four edges are clamped symmetrically to the thick aluminum bars by tightening the screws along each edge. The transversely isotropic piezoceramic square patches (T105-A4E-602 manufactured by Piezo Systems, Inc.) are employed as patch-based harvesters by bonding on the aluminum plate. The geometric, material, and electroelastic properties of the plate and the patch-based harvesters are given in Table 1.

Table 1. Geometric, material, and electroelastic properties.

Property	Aluminum	Piezoceramic patch
Length (mm)	580	72.4
Width (mm)	540	72.4
Thickness (mm)	1.9	0.267
Young's modulus (GPa)	65.1	66
Mass density (kg m^{-3})	2575	7800
Piezoelectric constant d_{31} (pm V^{-1})	–	−190
Permittivity constant $\bar{\varepsilon}_{33}^{S}$ (nF m^{-1})	–	10.38

Two harvester patches (labeled as PBEH-1 and PBEH-2) are attached on the front surface of the aluminum plate as shown in Figures 4 and 5(a). The patches come from the manufacturer with highly conductive electrode layers, and the attachment regions on the aluminum plate are electrically isolated with 3M Scotch 1601 Insulating Spray. The center of the PBEH-1 is located at 0.175 and 0.272 m away from the bottom left corner of the plate, whereas the center of the PBEH-2 is at 0.287 and 0.165 m away from the bottom left corner as can be seen in Figure 5(a). For the series connection of the two harvester patches displayed in Figure 5(b), the top electrode of PBEH-1 is connected to one end of the resistor, and the other end of the resistor is connected to the bottom electrode of PBEH-2, while the bottom electrode of PBEH-1 and the top electrode of PBEH-2 are connected together. In the case of the parallel connection, the top electrodes of PBEH-1 and PBEH-2 are directly connected to the one end of the resistor, and the bottom electrodes are connected to the other end of the resistor as displayed in Figure 5(c). The aluminum plate is excited by a linear sine-sweep signal over the bandwidth of 1-260 Hz through a modal shaker during the experimental FRF measurements. The shaker's rod is attached to 0.105 and 0.1 m away from the right bottom of the plate as shown in Figure 5(a). The dynamic point force acting on the plate is measured by a force transducer (PCB 208C01) mounted between the shaker's rod and the plate surface. The transverse velocity of the plate is measured by the laser Doppler vibrometer (LDV; Polytec PDV 100), and its target location is provided in Figure 5(a). A data acquisition system is used to record and analyze the signals coming from the force transducer, the LDV, and the voltage across the resistor. The experimental FRFs as the ratio of the velocity response-to-force input (velocity FRF) and the voltage across the resistive load-to-force input (voltage FRF) are obtained.

Downloaded from jim.sagepub.com at GEORGIA TECH LIBRARY on September 11, 2014

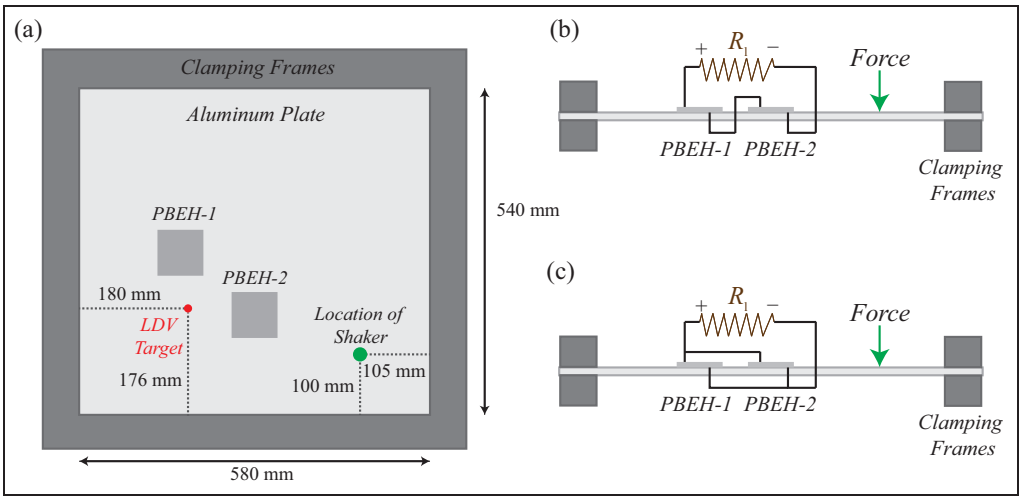

Figure 5. (a) Velocity measurement point (target of the LDV) and the excitation point (by the shaker); (b) series and (c) parallel connection configurations of the harvester patches.
LDV: laser Doppler vibrometer.

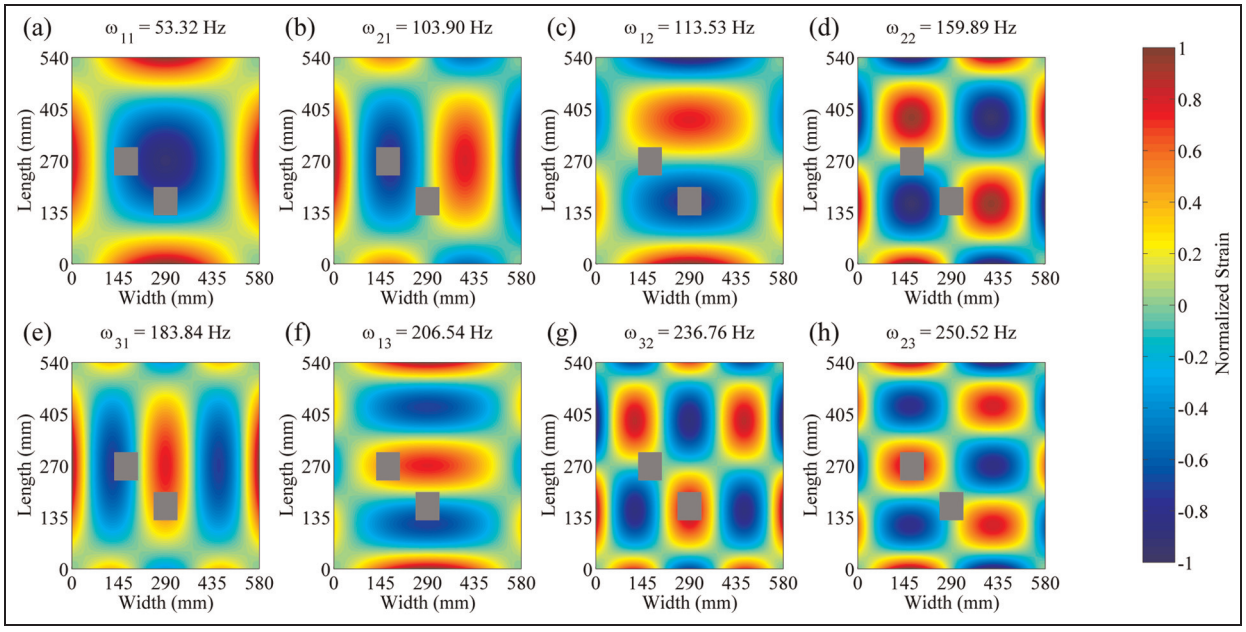

Figure 6. Normalized strain mode shapes: (a) first mode, (b) second mode, (c) third mode, (d) fourth mode, (e) fifth mode, (f) sixth mode, (g) seventh mode, and (h) eighth mode.

Strain distribution analysis

Current output of each harvester patch depends on the dynamic strain induced in the harvester patch as given by equation (5). In order to investigate the placement of harvester patches on the basis of vibration-mode dependent strain distribution (i.e. strain mode shape), the first eight undamped natural frequencies and displacement mode shapes of the aluminum plate are first calculated according to the properties given in Table 1. Then, the strain mode shapes are obtained by evaluating the second derivative (curvature) of the displacement mode shapes to form the Laplacian $\nabla^2\varphi$ (Aridogan et al., 2014). Figure 6 displays the normalized strain mode shapes along with undamped natural frequencies for the first eight modes of the uniform plate (for simplicity, by excluding the effects of piezoelectric patches since they are small). The gray shaded areas illustrate the regions covered by harvester patches PBEH-1 and PBEH-2.

As can be seen in Figure 6(a), PBEH-1 and PBEH-2 are located at moderate strain regions in the same phase for the first vibration mode of the plate. Besides, in the

Downloaded from jim.sagepub.com at GEORGIA TECH LIBRARY on September 11, 2014

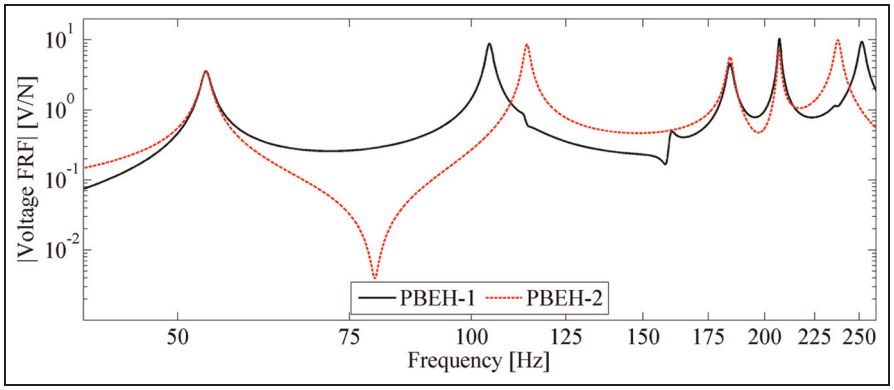

Figure 7. Comparison of the analytical voltage FRFs of harvester patches PBEH-1 and PBEH-2 in open-circuit conditions.
FRF: frequency response function.

second vibration of the plate as displayed in Figure 6(b), PBEH-1 is located over the high strain region, while PBEH-2 is located on the neighborhood of a strain node. Therefore, at the excitation frequency close to the second mode, one can expect more current output (therefore more power output) from PBEH-1 as compared to PBEH-2. For the case of the third vibration mode shown in Figure 6(c), PBEH-1 is located over the neighborhood of the strain node region, whereas PBEH-2 is at the center of the high strain region of the third vibration mode as opposed to the second mode. Hence, PBEH-2 can generate more current output at the excitation frequency close to the third vibration mode. The current outputs of PBEH-1 and PBEH-2 can be combined properly for excitation frequencies covering second and third vibration modes, yielding a single output and broadband performance. For higher vibration modes, depending on the number of the vibration mode, PBEH-1 and PBEH-2 are located in the high and low strain regions of the same or opposite phases. Note that at excitation frequencies around the fifth and the sixth vibration modes, the combination of current outputs can lead to cancellations due to out-of-phase behavior.

Analytical and experimental open-circuit FRFs

Before discussing the series and parallel connections of harvester patches, the analytical voltage FRF of each harvester patch close to open-circuit condition (for a resistive load of 1 MΩ) is simulated for the configuration illustrated in Figure 5(a) with the parameters provided in Table 1. Figure 7 presents the voltage FRFs with solid and dashed lines corresponding to PBEH-1 and PBEH-2, respectively. For excitation frequencies around the first vibration mode of the plate, the generated voltage amplitude of each harvester is similar because of comparable strain levels at the regions covered by the harvester patches for this mode in Figure 6(a). Additionally, as expected from strain distribution analysis, PBEH-1 generates significant amount of voltage output at excitation frequencies around the second vibration mode (103.9 Hz) and does not generate voltage at excitation frequencies near the third vibration mode (113.5 Hz). Likewise, the voltage output of PBEH-2 is not observed at the second mode, but significantly larger amount of voltage output is generated at excitation frequencies around the third vibration mode by PBEH-2. Similar trends in voltage outputs of PBEH-1 and PBEH-2 can also be observed in the seventh and eighth vibration modes in the voltage FRFs, which are also in agreement with strain distribution analysis provided in Figure 6(g) and (h).

Having discussed the independent open-circuit voltage FRF of each harvester patch, analytical simulations and experimental measurements are carried out for the series connection (Figure 5(b)) of PBEH-1 and PBEH-2. Figure 8 presents the experimental and analytical voltage FRFs close to open-circuit conditions (for a resistive load of 1 MΩ). The analytical prediction for the voltage FRF is in very good agreement with experimental data for the first eight vibration modes of the plate. For the analytical predictions, the electroelastic model explained in the previous sections is used along with modal damping ratio values extracted from the experimental data points.

By examining Figures 7 and 8 together, it can be observed that the series connection of PBEH-1 and PBEH-2 enables the combination of the voltage outputs at the second, third, seventh, and eighth vibration modes into a single voltage output, enabling energy harvesting from all vibration modes of interest. It is also worth mentioning that PBEH-1 and PBEH-2 are both located on the neighborhood of nodal strain region of the fourth vibration mode (see Figure 6(d)), and therefore, the voltage output at the fourth vibration mode is significantly smaller than that at other resonance frequencies.

During the experimental voltage FRF measurements, the vibration of the plate is also monitored at

Downloaded from jim.sagepub.com at GEORGIA TECH LIBRARY on September 11, 2014

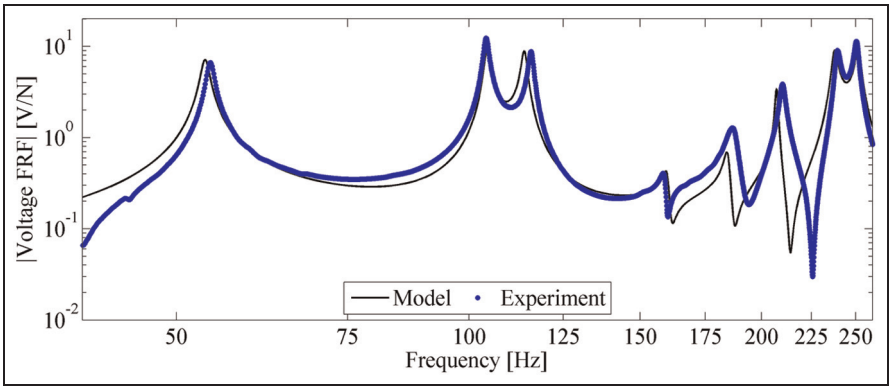

Figure 8. Comparison of the experimental and analytical voltage FRFs for series connection of harvesters in open-circuit conditions.
FRF: frequency response function.

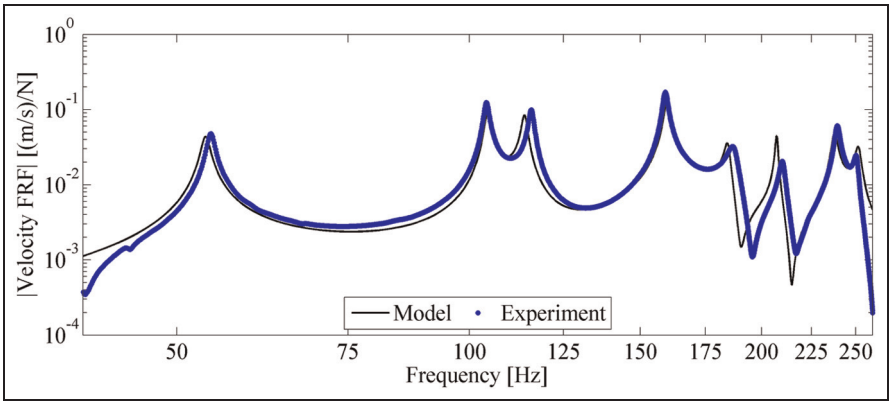

Figure 9. Comparison of the experimental and analytical velocity FRFs for series connection of harvesters in open-circuit conditions.
FRF: frequency response function.

the target point with LDV as shown in Figures 4 and 5(a). Experimental velocity FRF is obtained from the outputs of LDV and force transducer, while the analytical velocity FRF is simulated for the same target point using the coupled electroelastic model. Figure 9 displays the experimental and analytical velocity FRFs in open-circuit conditions, and it can be seen that analytical model predicts the vibration response of the plate very well for the first eight modes of the plate.

For the case of parallel connection of harvester patches, PBEH-1 and PBEH-2 are configured as displayed in Figure 5(c). The experimentally measured and analytically predicted voltage and velocity FRFs are shown in Figures 10 and 11, respectively. The experimental voltage and velocity FRFs are very well predicted by the analytical model. Similar to the results of series connection, using two parallel-connected patches located at different positions on the host plate yielded combined energy harvesting from multiple vibration modes of the thin plate.

Analytical and experimental resonant voltage and power output diagrams

To investigate the variation of electrical outputs with different load resistance values, experimental measurements and analytical simulations of voltage FRFs are carried out for a set of resistive loads listed in Table 2. The 18 resistive loads used in the test range from 0.012 kΩ (near short-circuit condition) to 991 kΩ (near open-circuit condition). Having obtained the voltage FRFs analytically and experimentally, the peak voltage outputs at the open-circuit resonance frequencies of the first eight vibration modes are picked from the experimental and analytical data points corresponding to the each load resistance value. Figure 12 presents the variation of peak voltage output with load resistance for the first eight vibration modes of the aluminum plate. The peak voltage amplitudes monotonically increase up to a certain level near open-circuit conditions and then become saturated as a common trend for all vibration modes of interest. Expectedly, the voltage output of

Downloaded from jim.sagepub.com at GEORGIA TECH LIBRARY on September 11, 2014

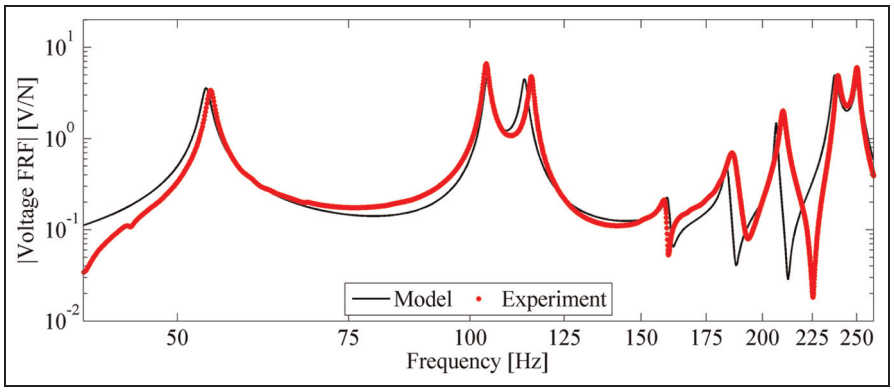

Figure 10. Comparison of the experimental and analytical voltage FRFs for parallel connection of harvesters in open-circuit conditions.
FRF: frequency response function.

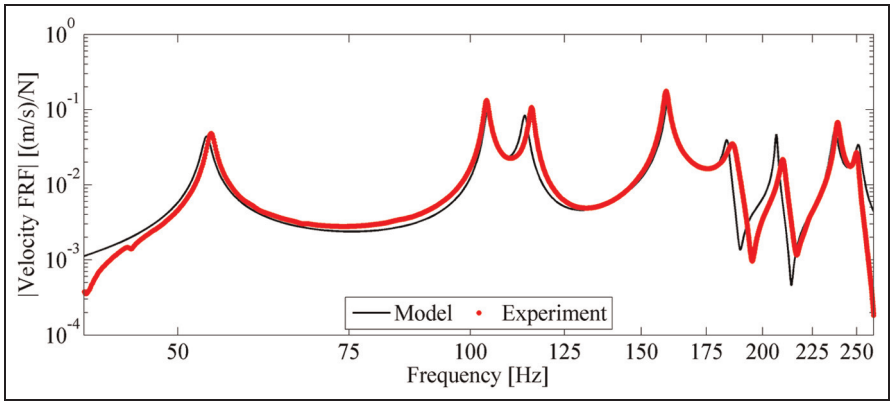

Figure 11. Comparison of the experimental and analytical velocity FRFs for parallel connection of harvesters in open-circuit conditions.
FRF: frequency response function.

Table 2. Set of load resistance (R_l) values used in the experiments.

Resistance order	Resistance value (kΩ)	Resistance order	Resistance value (kΩ)	Resistance order	Resistance value (kΩ)
1	0.012	7	3.83	13	48.1
2	0.057	8	5.56	14	100
3	0.219	9	9.75	15	330
4	0.464	10	14.7	16	472
5	1.18	11	21.7	17	695
6	2.68	12	32.5	18	991

series connection is larger than that of the parallel connection near open-circuit condition, whereas close to short-circuit condition, the voltage amplitudes of parallel connection case are larger than those of series connection counterpart. Overall, the analytical results exhibit very good agreement with the experimental data for both the series and parallel connections of harvester patches.

The experimental and analytical power FRFs are then calculated for each resistive load by using the voltage FRFs. Similar to the previous discussion on peak voltage amplitudes, the peak power outputs are extracted at the open-circuit resonance frequencies of the first eight vibration modes of the plate. Variations of peak power amplitudes for excitations at the first eight vibration modes are plotted versus load resistance values in Figure 13. The power curves have similar trends for each vibration mode, exhibiting an optimum resistive load for the maximum peak power output. It can be observed that the optimal load resistance value

Downloaded from jim.sagepub.com at GEORGIA TECH LIBRARY on September 11, 2014

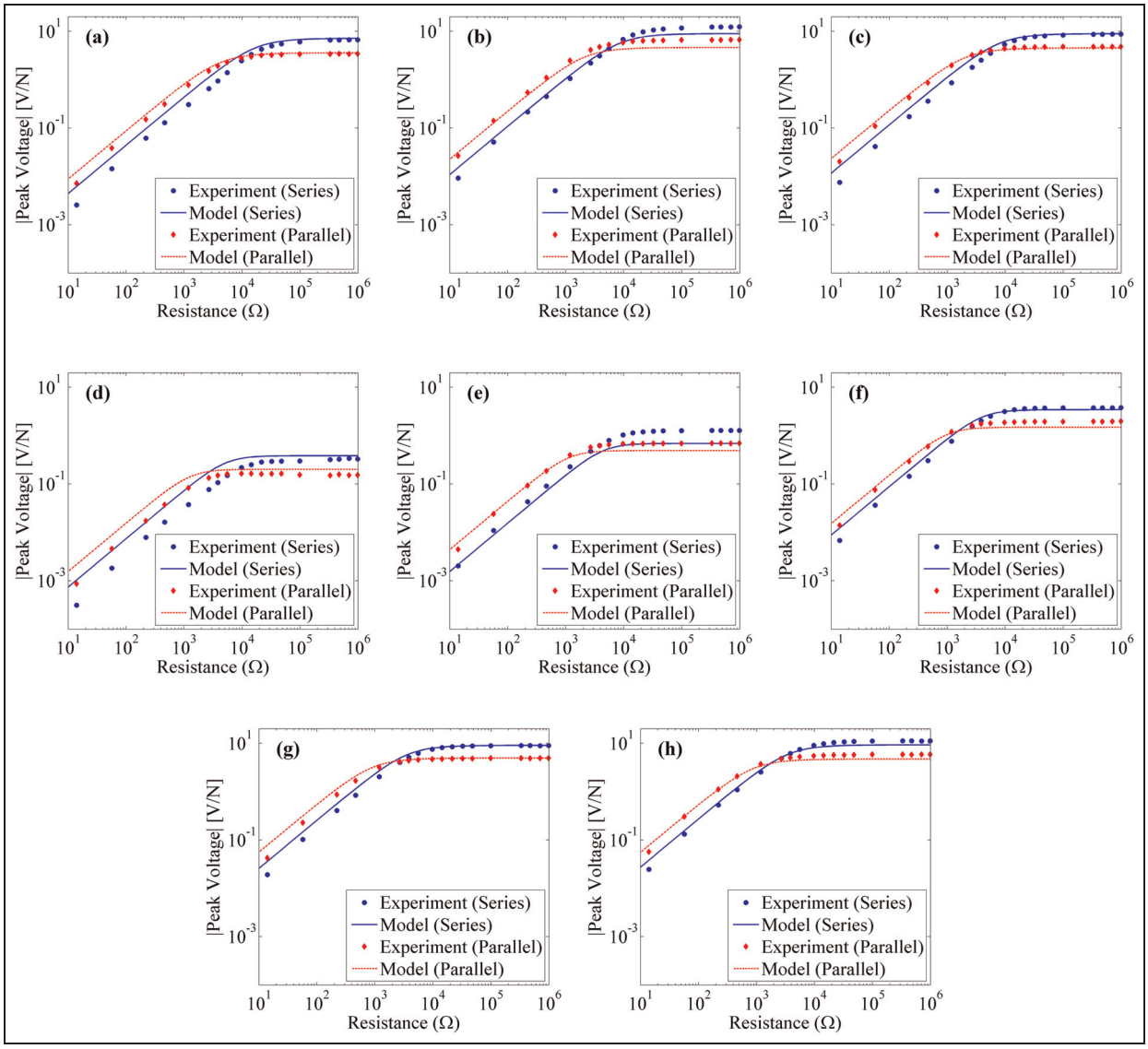

Figure 12. Variations of resonant voltage amplitudes of series and parallel connections of harvesters with load resistance for excitations at the open-circuit resonance frequencies: (a) first mode, (b) second mode, (c) third mode, (d) fourth mode, (e) fifth mode, (f) sixth mode, (g) seventh mode, and (h) eighth mode.

of parallel connection configuration is smaller than that of series connection case. Note that strain mode shape–related cancellations may differ in the output values for the series and parallel connection cases. The modal power output trends are in agreement with the modal strain distributions given in Figure 6. The analytical predictions agree well with the experimental data in Figure 13 for a wide range of resistive loads and vibration modes.

Conclusion

This article presents electroelastic modeling, experimental validation, and performance investigation of MPBEHs integrated to thin plates. Thin plate-like structures with patch-based piezoelectric harvesters offer many advantages over standard cantilevered energy harvesters due to their closely spaced vibration modes and common applications in engineering systems ranging from aerospace to marine structures. Furthermore, the use of standard cantilevered energy harvesters may not be convenient for such thin plate–based structures due to space limitations and mass loading effects. However, integrated piezoelectric patches can easily be implemented for enabling self-powered sensors in the neighborhood of plate structures with different boundary conditions. In this work, electroelastic models of series and parallel connections of MPBEHs attached on thin plates are presented along with experimental investigations. The electroelastic model of harvester patches together with the host plate is derived in physical coordinates based on a

Downloaded from jim.sagepub.com at GEORGIA TECH LIBRARY on September 11, 2014

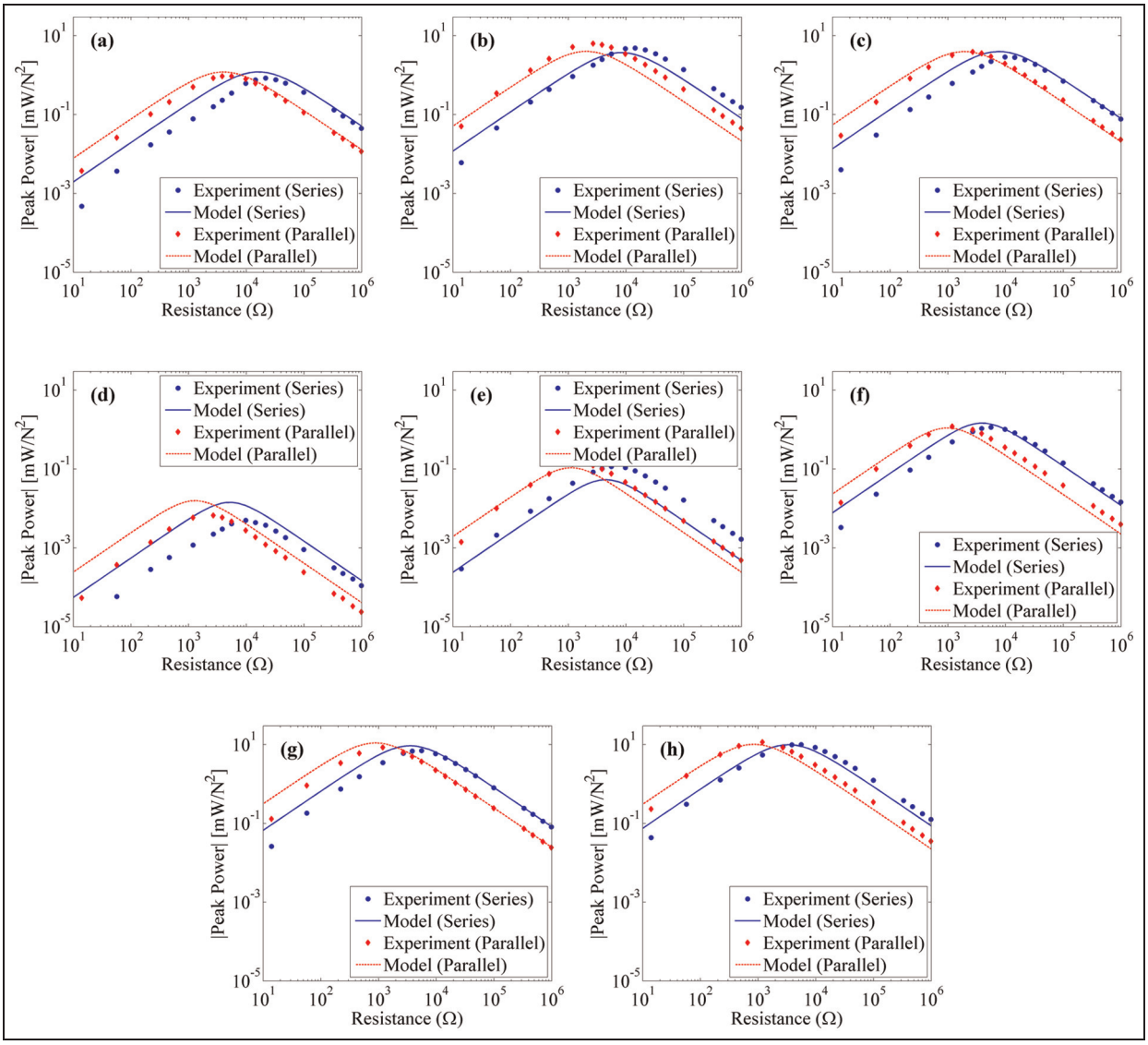

Figure 13. Variations of resonant power amplitudes of series and parallel connections of harvesters with load resistance for excitations at the open-circuit resonance frequencies: (a) first mode, (b) second mode, (c) third mode, (d) fourth mode, (e) fifth mode, (f) sixth mode, (g) seventh mode, and (h) eighth mode.

distributed-parameter modeling approach. By transforming the coupled electroelastic equations from physical coordinates to modal coordinates for a fully clamped thin plate, analytical solutions are obtained. Steady-state coupled structural and electrical response expressions are formulated for the transversely applied point force excitations in the cases of series and parallel connections of harvester patches in the presence of a resistive load. Electroelastic FRFs relating the voltage output and vibration response to force input are derived for multiple vibration modes of thin plates for the series and parallel connection cases. Model validation experiments are presented with an experimental case study, and it is shown that the analytical predictions and experimental measurements of voltage and velocity FRFs are in very good agreement for multiple vibration modes of the thin plate. Using the experimental measurements and analytical simulations, the harvested power and voltage output across the resistive load are explored for the first eight vibration modes. The experimental and analytical results presented in this article show that using MPBEHs can lead to effective broadband energy harvesting on thin plates, and the electroelastic models developed herein can be used for design and performance optimization.

Declaration of conflicting interests

The authors declared no potential conflicts of interest with respect to the research, authorship, and/or publication of this article.

Funding

This study received financial support from Koç University TÜPRAŞ Energy Center (KÜTEM).

Downloaded from jim.sagepub.com at GEORGIA TECH LIBRARY on September 11, 2014

References

Anton SR and Sodano HA (2007) A review of power harvesting using piezoelectric materials (2003–2006). *Smart Materials and Structures* 16: R1–R21.

Aridogan U, Basdogan I and Erturk A (2014) Analytical modeling and experimental validation of a structurally integrated piezoelectric energy harvester on a thin plate. *Smart Materials and Structures* 23: 045039.

Beeby SP, Torah RN, Tudor MJ, et al. (2007) A micro electromagnetic generator for vibration energy harvesting. *Journal of Micromechanics and Microengineering* 17: 1257.

Beeby SP, Tudor MJ and White NM (2006) Energy harvesting vibration sources for microsystems applications. *Measurement Science & Technology* 17: R175–R195.

Behrens S, Fleming AJ and Moheimani SOR (2003) A broadband controller for shunt piezoelectric damping of structural vibration. *Smart Materials and Structures* 12: 18–28.

Brufau-Penella J, Puig-Vidal M, Giannone P, et al. (2008) Characterization of the harvesting capabilities of an ionic polymer metal composite device. *Smart Materials and Structures* 17: 015009.

Carrara M, Cacan MR, Toussaint J, et al. (2013) Metamaterial-inspired structures and concepts for elastoacoustic wave energy harvesting. *Smart Materials and Structures* 22: 065004.

Casadei F, Ruzzene M, Dozio L, et al. (2010) Broadband vibration control through periodic arrays of resonant shunts: experimental investigation on plates. *Smart Materials and Structures* 19: 015002.

Chiu Y and Tseng VFG (2008) A capacitive vibration-to-electricity energy converter with integrated mechanical switches. *Journal of Micromechanics and Microengineering* 18: 104004.

Cook-Chennault KA, Thambi N and Sastry AM (2008a) Powering MEMS portable devices—a review of non-regenerative and regenerative power supply systems with special emphasis on piezoelectric energy harvesting systems. *Smart Materials and Structures* 17: 043001.

Cook-Chennault KA, Thambi N, Bitetto MA, et al. (2008b) Piezoelectric energy harvesting: a green and clean alternative for sustained power production. *Bulletin of Science, Technology & Society* 28: 496–509.

De Marqui C, Erturk A and Inman DJ (2009) An electromechanical finite element model for piezoelectric energy harvester plates. *Journal of Sound and Vibration* 327: 9–25.

Elvin NG and Elvin AA (2009) A coupled finite element—circuit simulation model for analyzing piezoelectric energy generators. *Journal of Intelligent Material Systems and Structures* 20: 587–595.

Erturk A (2011) Piezoelectric energy harvesting for civil infrastructure system applications: moving loads and surface strain fluctuations. *Journal of Intelligent Material Systems and Structures* 22: 1959–1973.

Erturk A (2012) Assumed-modes modeling of piezoelectric energy harvesters: Euler–Bernoulli, Rayleigh, and Timoshenko models with axial deformations. *Computers & Structures* 106–107: 214–227.

Erturk A and Inman DJ (2008a) A distributed parameter electromechanical model for cantilevered piezoelectric energy harvesters. *Journal of Vibration and Acoustics: Transactions of the ASME* 130: 041002–041015.

Erturk A and Inman DJ (2008b) Issues in mathematical modeling of piezoelectric energy harvesters. *Smart Materials and Structures* 17: 065016.

Erturk A and Inman DJ (2009) An experimentally validated bimorph cantilever model for piezoelectric energy harvesting from base excitations. *Smart Materials and Structures* 18: 025009.

Erturk A and Inman DJ (2011a) Parameter identification and optimization in piezoelectric energy harvesting: analytical relations, asymptotic analyses, and experimental validations. *Proceedings of the Institution of Mechanical Engineers, Part I: Journal of Systems and Control Engineering* 225: 485–496.

Erturk A and Inman DJ (2011b) *Piezoelectric Energy Harvesting*. Chichester: John Wiley & Sons, Ltd.

Erturk A, Bilgen O and Inman DJ (2008) Power generation and shunt damping performance of a single crystal lead magnesium niobate-lead zirconate titanate unimorph: analysis and experiment. *Applied Physics Letters* 93: 224102–224103.

Erturk A, Hoffmann J and Inman DJ (2009a) A piezomagnetoelastic structure for broadband vibration energy harvesting. *Applied Physics Letters* 94: 254102–254103.

Erturk A, Renno JM and Inman DJ (2009b) Modeling of piezoelectric energy harvesting from an L-shaped beam-mass structure with an application to UAVs. *Journal of Intelligent Material Systems and Structures* 20: 529–544.

Fein OM (2008) A model for piezo-resistive damping of two-dimensional structures. *Journal of Sound and Vibration* 310: 865–880.

Ferrari M, Ferrari V, Guizzetti M, et al. (2008) Piezoelectric multifrequency energy converter for power harvesting in autonomous microsystems. *Sensors and Actuators A: Physical* 142: 329–335.

Forward RL (1979) Electronic damping of vibrations in optical structures. *Applied Optics* 18: 690–697.

Friswell MI and Adhikari S (2010) Sensor shape design for piezoelectric cantilever beams to harvest vibration energy. *Journal of Applied Physics* 108: 014901–014906.

Huan X, Yuantai H and Qing-Ming W (2008) Broadband piezoelectric energy harvesting devices using multiple bimorphs with different operating frequencies. *IEEE Transactions on Ultrasonics, Ferroelectrics and Frequency Control* 55: 2104–2108.

Huang S-C and Lin K-A (2012) A novel design of a map-tuning piezoelectric vibration energy harvester. *Smart Materials and Structures* 21: 085014.

Kim J and Jung Y-C (2006) Broadband noise reduction of piezoelectric smart panel featuring negative-capacitive-converter shunt circuit. *Journal of the Acoustical Society of America* 120: 2017–2025.

Kim J and Kim J-H (2004) Multimode shunt damping of piezoelectric smart panel for noise reduction. *Journal of the Acoustical Society of America* 116: 942–948.

Koshigoe S and Murdock JW (1993) A unified analysis of both active and passive damping for a plate with piezoelectric transducers. *Journal of the Acoustical Society of America* 93: 346–355.

Lee C, Lim YM, Yang B, et al. (2009) Theoretical comparison of the energy harvesting capability among various electrostatic mechanisms from structure aspect. *Sensors and Actuators A: Physical* 156: 208–216.

Downloaded from jim.sagepub.com at GEORGIA TECH LIBRARY on September 11, 2014

Lee S and Youn BD (2011) A new piezoelectric energy harvesting design concept: multimodal energy harvesting skin. *IEEE Transactions on Ultrasonics, Ferroelectrics and Frequency Control* 58: 629–645.

Lien IC and Shu YC (2012) Array of piezoelectric energy harvesting by the equivalent impedance approach. *Smart Materials and Structures* 21: 082001.

Lin HC, Wu PH, Lien IC, et al. (2013) Analysis of an array of piezoelectric energy harvesters connected in series. *Smart Materials and Structures* 22: 094026.

Manzoni S, Moschini S, Redaelli M, et al. (2012) Vibration attenuation by means of piezoelectric transducer shunted to synthetic negative capacitance. *Journal of Sound and Vibration* 331: 4644–4657.

Moheimani SOR and Behrens S (2004) Multimode piezoelectric shunt damping with a highly resonant impedance. *IEEE Transactions on Control Systems Technology* 12: 484–491.

Niederberger D, Fleming A, Moheimani SOR, et al. (2004) Adaptive multi-mode resonant piezoelectric shunt damping. *Smart Materials and Structures* 13: 1025.

Richard T, Magnet C, Richard C, et al. (2011) Board multimodal vibration control using piezoelectric synchronized switch damping techniques. *Journal of Vibration and Control* 17: 845–856.

Roundy S, Wright PK and Rabaey J (2003) A study of low level vibrations as a power source for wireless sensor nodes. *Computer Communications* 26: 1131–1144.

Rupp CJ, Evgrafov A, Maute K, et al. (2009) Design of piezoelectric energy harvesting systems: a topology optimization approach based on multilayer plates and shells. *Journal of Intelligent Material Systems and Structures* 20: 1923–1939.

Saravanos DA (1999) Damped vibration of composite plates with passive piezoelectric-resistor elements. *Journal of Sound and Vibration* 221: 867–885.

Shahruz SM (2006) Design of mechanical band-pass filters with large frequency bands for energy scavenging. *Mechatronics* 16: 523–531.

Song HJ, Choi Y-T, Purekar AS, et al. (2009) Performance evaluation of multi-tier energy harvesters using macro-fiber composite patches. *Journal of Intelligent Material Systems and Structures* 20: 2077–2088.

Wang L and Yuan FG (2008) Vibration energy harvesting by magnetostrictive material. *Smart Materials and Structures* 17: 045009.

Wang ZL and Song J (2006) Piezoelectric nanogenerators based on zinc oxide nanowire arrays. *Science* 312: 242–246.

Xing YF and Liu B (2009) New exact solutions for free vibrations of thin orthotropic rectangular plates. *Composite Structures* 89: 567–574.

Yang Y and Tang L (2009) Equivalent circuit modeling of piezoelectric energy harvesters. *Journal of Intelligent Material Systems and Structures* 20: 2223–2235.

Zhao S and Erturk A (2013) Electroelastic modeling and experimental validations of piezoelectric energy harvesting from broadband random vibrations of cantilevered bimorphs. *Smart Materials and Structures* 22: 015002.

Zhu D, Beeby S, Tudor J, et al. (2012) Vibration energy harvesting using the Halbach array. *Smart Materials and Structures* 21: 075020.

Downloaded from jim.sagepub.com at GEORGIA TECH LIBRARY on September 11, 2014